Generic Miniband Structure of Graphene on a Hexagonal Substrate

J. R. Wallbank,[1] A. A. Patel,[1,2] M. Mucha-Kruczyński,[1] A. K. Geim,[3] and V. I. Fal'ko[1,4]

[1]*Department of Physics, Lancaster University, Lancaster, LA1 4YB, UK*
[2]*Department of Physics, Indian Institute of Technology Kanpur, Kanpur 208016, India*
[3]*Centre for Mesoscience and Nanotechnology, University of Manchester, Manchester M13 9PL, UK*
[4]*DPMC, University of Geneva, 24 Quai Ernest-Ansermet, CH1211 Genéve 4, Switzerland*

(Dated: November 21, 2012)

We present a symmetry based classification of generic miniband structures for electrons in graphene placed on substrates with the hexagonal Bravais symmetry. In particular, we identify conditions at which the first moiré miniband is separated from the rest of the spectrum by either one or a group of three isolated mini Dirac points and is not obscured by dispersion surfaces coming from other minibands. In such cases the Hall coefficient exhibits two distinct alternations of its sign as a function of charge carrier density.

PACS numbers: 73.22.Pr,73.21.Cd,73.43.-f

Recently, it has been demonstrated that the electronic quality of graphene-based devices can be dramatically improved by placing graphene on an atomically flat crystal surface such as hexagonal boron nitride (hBN) [1–7]. At the same time, graphene's electronic spectrum also becomes modified, acquiring a complex, energy-dependent form caused by incommensurability between the graphene and substrate crystal lattices [8–10]. In particular, for graphene placed on hBN, the difference between their lattice constants and crystallographic misalignment generate a hexagonal periodic structure known as a moiré pattern [2, 3, 8–10]. The resulting periodic perturbation, usually referred to as a superlattice, acts on graphene's charge carriers and leads to multiple minibands and the generation of secondary Dirac-like spectra. The resulting new Dirac fermions present yet another case where graphene allows mimicking of QED phenomena under conditions that cannot be achieved in particle physics experiments. In contrast to relativistic particles in free space, the properties of secondary Dirac fermions in graphene can be affected by a periodic sublattice symmetry breaking and modulation of carbon-carbon hopping amplitudes, in addition to a simple potential modulation. The combination of different modulation mechanisms results in a multiplicity of possible outcomes for the moiré miniband spectrum in graphene which we systematically investigate in this Letter.

To describe the effect of a substrate on electrons in graphene at a distance, d, much larger than the spacing, a, between carbon atoms in graphene's honeycomb lattice, we use the earlier observation [8–14] that, at $d \gg a$ the lateral variation of the wavefunctions of the p^z carbon orbitals is smooth on the scale of a. This is manifested in the comparable sizes of the skew and vertical hopping in graphite and permits an elegant continuum-model description [11–14] of the interlayer coupling in twisted bilayers and the resulting band structure. A similar idea applied to graphene on a h-BN substrate [8–10] suggests that a substrate perturbation for Dirac electrons in graphene can be described in terms of simple harmonic functions corresponding to the six smallest reciprocal lattice vectors of the moiré superlattice.

Below, we shall use a similar approach to analyse the generic properties of moiré minibands for electrons in graphene subjected to a substrate with a hexagonal Bravais lattice with a slightly different lattice constant of $(1+\delta)\sqrt{3}a$, $|\delta| \ll 1$, compared to that of $\sqrt{3}a$ for graphene, and a small misalignment angle, $\theta \ll 1$. The moiré pattern harmonics are described by vectors $\boldsymbol{b}_m = \hat{R}_{2\pi m/6}\boldsymbol{b}_0$ $(m = 0, 1...5)$, which can be obtained by the anticlockwise rotation, $\hat{R}_{2\pi m/6}$, of $\boldsymbol{b}_0 = \left[1-(1+\delta)\hat{R}_\theta\right]\left(0, \frac{-4\pi}{3a}\right)$ with $|\boldsymbol{b}_0| \equiv b \approx \frac{4\pi}{3a}\sqrt{\delta^2+\theta^2}$. For a substrate with a simple hexagonal lattice or a honeycomb lattice with two identical atoms, the perturbation created for graphene electrons is inversion-symmetric. For a honeycomb substrate where one of the atoms would affect graphene electrons stronger than the other (e.g. such as h-BN, for which the occupancy and size of the p^z orbitals are different) the moiré potential can be modelled as a combination of a dominant inversion-symmetric part with the addition of a small inversion-asymmetric perturbation,

$$\begin{aligned}\hat{H} = v\boldsymbol{p}\cdot\boldsymbol{\sigma} + u_0 vbf_1(\boldsymbol{r}) + u_3 vbf_2(\boldsymbol{r})\sigma_3\tau_3 + u_1 v\left[\boldsymbol{l}_z \times \nabla f_2(\boldsymbol{r})\right]\cdot\boldsymbol{\sigma}\tau_3 + u_2 v\nabla f_2(\boldsymbol{r})\cdot\boldsymbol{\sigma}\tau_3 \\ + \tilde{u}_0 vbf_2(\boldsymbol{r}) + \tilde{u}_3 vbf_1(\boldsymbol{r})\sigma_3\tau_3 + \tilde{u}_1 v\left[\boldsymbol{l}_z \times \nabla f_1(\boldsymbol{r})\right]\cdot\boldsymbol{\sigma}\tau_3 + \tilde{u}_2 v\nabla f_1(\boldsymbol{r})\cdot\boldsymbol{\sigma}\tau_3. \quad (1)\end{aligned}$$

The Hamiltonian, $\hat{H}$, acts on four-component wavefunctions, $(\Psi_{AK}, \Psi_{BK}, \Psi_{BK'}, -\Psi_{AK'})^T$, describing the

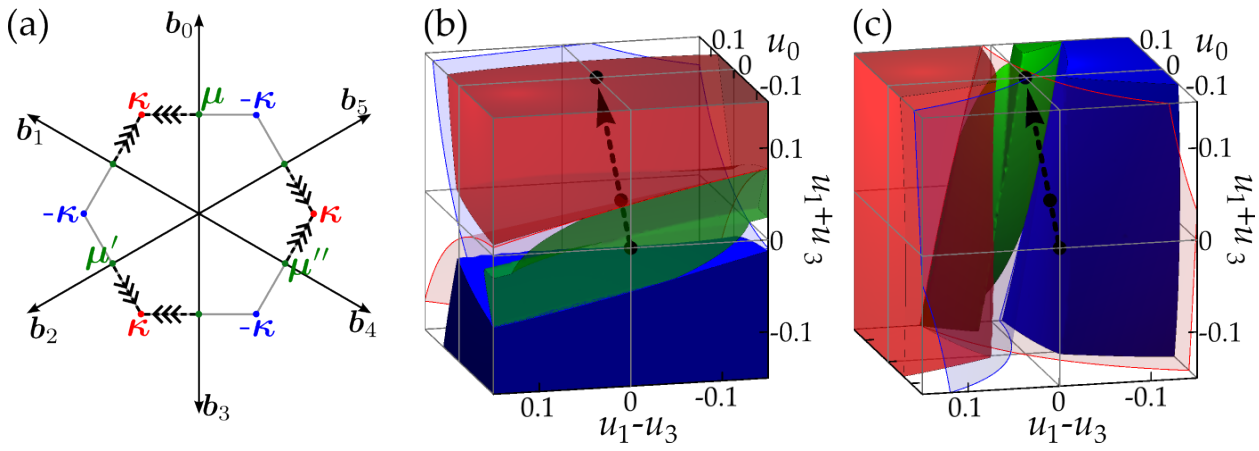

FIG. 1: (a) The hexagonal Brillouin zone for the moiré superlattice. (b) Three volumes in the space of the moiré superlattice parameters where the edge of the first miniband, in graphene's valence band, contains an isolated mDP at the $\boldsymbol{\kappa}$-point (red) or the $-\boldsymbol{\kappa}$-point (blue) or three isolated mDPs at the sBZ edge (green). Parameters for which the $\pm\boldsymbol{\kappa}$-point is triple degenerate are shown by the red and blue surfaces. (c)The same for the conduction band in graphene.

electron amplitudes on graphene sublattices A and B and in two principal valleys, K and K'. It is written in terms of direct products $\sigma_i\tau_j$, of Pauli matrices σ_i and τ_j separately acting on sublattice and valley indices. The first term in $\hat{H}$ is the Dirac part, with $\boldsymbol{p}=-i\nabla-e\boldsymbol{A}$ describing the momentum relative to the centre of the corresponding valley, with $\nabla\times\boldsymbol{A}=B$. The rest of the first line in Eq. (1) describes the inversion-symmetric part of the moiré perturbation, whereas the second line takes into account its inversion-asymmetric part. In the first line, the first term, with $f_1(\boldsymbol{r})=\sum_{m=0\ldots5}e^{i\boldsymbol{b}_m\cdot\boldsymbol{r}}$, describes a simple potential modulation. The second term, with $f_2(\boldsymbol{r})=i\sum_{m=0\ldots5}(-1)^m e^{i\boldsymbol{b}_m\cdot\boldsymbol{r}}$, accounts for the A-B sublattice asymmetry, locally imposed by the substrate. Then the third term, with unit vector $\boldsymbol{l}_z$, describes the influence of the substrate on the A-B hopping: consequently [15–17], this term can be associated with a pseudo-magnetic field, $e\beta=\pm u_1 b^2 f_2(\boldsymbol{r})$, which has opposite signs in valleys K and K'. All parameters $|u_i|\ll 1$ in Eq. (1) are dimensionless and $vb\approx 2\pi\sqrt{\delta^2+\theta^2}\gamma_0$, where $\gamma_0\approx 3\,\mathrm{eV}$ is the nearest neighbour hopping integral in the Slonczewski-Weiss tight binding model [18]. Concerning the inversion-asymmetric part, the second line in Eq. (1), we assume that $|\tilde{u}_i|\ll|u_i|$. Note that the last term in each line can be gauged away using $\boldsymbol{\psi}\to e^{-i\tau_3(u_2 f_2+\tilde{u}_2 f_1)}\boldsymbol{\psi}$.

In the absence of a magnetic field, the Hamiltonian Eq. (1) obeys time-reversal symmetry, which follows from both σ_i and τ_i changing sign upon the transformation $t\to -t$ [19]. As a result, $\epsilon_{\boldsymbol{K}+\boldsymbol{p}}=\epsilon_{\boldsymbol{K}'-\boldsymbol{p}}$ and we limit the discussion of minibands to the K valley. Moreover, using the commutation properties of σ_i one can establish that

$$\epsilon^{u_0,u_1,u_3}_{\boldsymbol{K}+\boldsymbol{p}}=-\epsilon^{-u_0,-u_1,u_3}_{\boldsymbol{K}-\boldsymbol{p}}=-\epsilon^{-u_0,u_1,-u_3}_{\boldsymbol{K}+\boldsymbol{p}}=\epsilon^{u_0,-u_1,-u_3}_{\boldsymbol{K}-\boldsymbol{p}}. \quad (2)$$

To calculate the miniband spectrum for $\hat{H}$ in Eq. (1) we perform zone folding (in the graphene K valley) bringing states with momenta related by the reciprocal lattice vectors $n_1\boldsymbol{b}_1+n_2\boldsymbol{b}_2$ of the moiré pattern to the same point of the superlattice Brillouin zone (sBZ) in Fig. 1(a). Then, we calculate the matrix elements of $\hat{H}$ between those states and diagonalise the corresponding Heisenberg matrix numerically exploring the parametric space (u_0,u_1,u_3) of the moiré superlattice shown in Fig 1 (b,c). The size of the matrix is chosen to guarantee the convergence of the calculated energies for the three lowest minibands in both the conduction band ($s=+1$) and the valence band ($s=-1$). Below, we discuss the generic features of the moiré miniband spectra for the characteristic points in the parametric space (u_0,u_1,u_3), identified by black dots in Fig. 1(b,c), using both the numerically calculated dispersion surfaces in Fig. 2 and analytical perturbation theory analysis.

For the zero-energy Dirac point in graphene, there are only the original $\boldsymbol{p}=0$ states in each valley that appear at $\epsilon=0$ upon zone folding. For all three characteristic spectra shown in Fig. 2, for the inversion symmetric moiré perturbation, the gapless Dirac spectrum persists at low energies near the conduction-valence band edge with almost unchanged Dirac velocity, $\left[1+O(u^2)\right]v$, whereas the the inversion asymmetric terms are able [10] to open a minigap.

For the point $\boldsymbol{\mu}=\boldsymbol{b}_0/2$ on the edge of the first sBZ, zone folding brings together two degenerate plane wave states, $|\boldsymbol{\mu}+\boldsymbol{q}\rangle$ and $|\boldsymbol{\mu}+\boldsymbol{b}_3+\boldsymbol{q}\rangle$. The splitting of these degenerate states by the moiré potential in Eq. (1) can be studied using degenerate perturbation theory. The corresponding 2×2 matrix, expanded in small deviation $\boldsymbol{q}$ of the electron momentum from each of the three sBZ

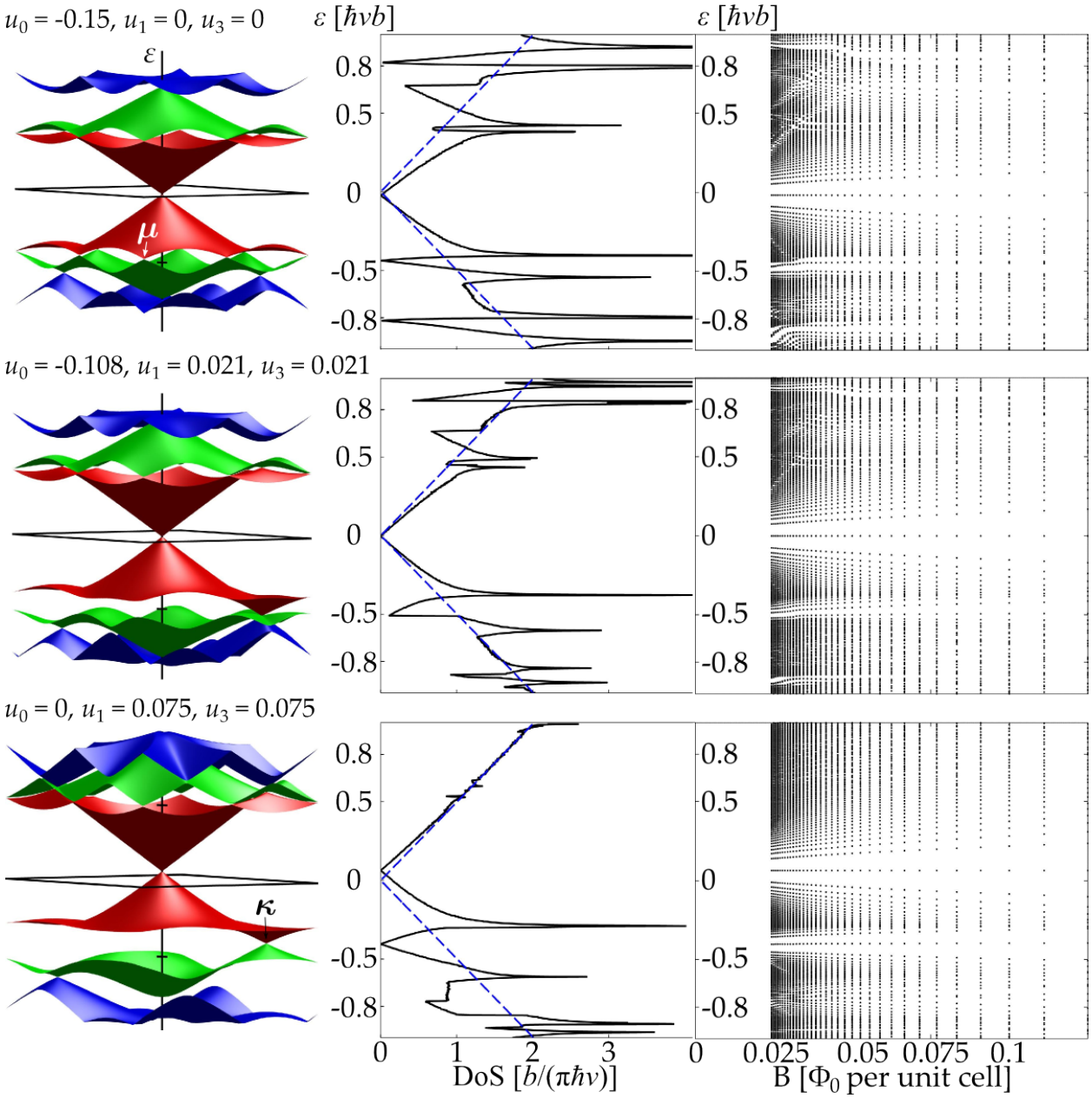

FIG. 2: Numerically calculated moiré miniband (left), the corresponding density of states (centre), and Landau level spectrum (right) for electrons in the vicinity of graphene's K point

$\boldsymbol{\mu}$-points [20] has the form

$$H_{\boldsymbol{\mu}+\boldsymbol{q}} = vb\begin{pmatrix} E_{\boldsymbol{\mu}} + s\frac{q_y}{b} & H_{12} \\ H_{12}^* & E_{\boldsymbol{\mu}} - s\frac{q_y}{b}\end{pmatrix},$$

$$E_{\boldsymbol{\mu}} \approx \frac{s}{2} + \frac{sq_x^2}{b^2},$$

$$H_{12} \approx (su_1 - u_3) - i(s\tilde{u}_1 - \tilde{u}_3) + 2\frac{q_x}{b}(u_0 + i\tilde{u}_0). \quad (3)$$

For the inversion-symmetric perturbation, the dispersion relation resulting from Eq. (3) contains an anisotropic mini Dirac point (mDP) [8, 21, 22] with Dirac velocity component $\approx 2u_0 v$ in the direction of the sBZ edge and $\approx v$ in the perpendicular direction. This feature is clearly seen at the $\boldsymbol{\mu}$-point of the first moiré miniband in the valence band, in the top row of Fig. 2. Note that the electron spectrum is not symmetric between the valence and conduction bands and that the mDPs at the $\boldsymbol{\mu}$-point in the conduction band are obscured by an overlapping spectral branch.

Moving in parameter space, e.g., along the line shown in Fig. 1(b), the positions of the three anisotropic mDPs shift along the sBZ edge towards the sBZ corners: either $\boldsymbol{\kappa} = (\boldsymbol{b}_4 + \boldsymbol{b}_5)/3$, or $-\boldsymbol{\kappa}$, as shown by arrowed lines in Fig. 1(a). In general, a spectrum with three iso-

lated mDPs at the sBZ edge is typical for the green volume in the parameter space in Fig. 1(b) for the valence band, or Fig. 1(c) for the conduction band. In contrast, for (u_0, u_1, u_3) in the clear part of the parameter space, mDPs on the edge of the first sBZ are overshadowed by an overlapping spectral branch, as is the case on the conduction band side for all three cases shown in Fig. 2.

For the points in Fig. 1(b,c) on the red and blue surfaces, the three mDPs reach the $\boldsymbol{\kappa}$-point, forming a triple degenerate band crossing, as in the valence band spectrum shown in the middle row of Fig. 2, which can be traced using the perturbation theory analysis of the band crossing at $\boldsymbol{\kappa}$ discussed below.

The third line in Fig. 2 shows the third type of spectrum of moiré minibands, characteristic for the red and blue volumes of the parameter space in Fig. 1. The characteristic feature of such spectra consists in a single isolated mDP, at the $\pm\boldsymbol{\kappa}$-point, in the valence band (Fig. 2(b)) or the conduction band (Fig. 1(c)).

For the $\boldsymbol{\kappa}$ and $-\boldsymbol{\kappa}$-points, zone folding brings together three degenerate plane wave states, $|\zeta(\boldsymbol{\kappa}+\boldsymbol{q})\rangle$, $|\zeta(\boldsymbol{\kappa}+\boldsymbol{b}_1+\boldsymbol{q})\rangle$, and $|\zeta(\boldsymbol{\kappa}+\boldsymbol{b}_2+\boldsymbol{q})\rangle$ (where $\zeta=\pm$), whose splitting is determined by

$$H_{\zeta(\boldsymbol{\kappa}+\boldsymbol{q})}=vb\begin{pmatrix}\frac{s}{\sqrt{3}}+\frac{sq_x}{b} & e^{i\frac{2\pi}{6}}w_\zeta & e^{-i\frac{2\pi}{6}}w_\zeta^* \\ e^{-i\frac{2\pi}{6}}w_\zeta^* & \frac{s}{\sqrt{3}}-s\frac{q_x-\sqrt{3}q_y}{2b} & e^{i\frac{2\pi}{6}}w_\zeta \\ e^{i\frac{2\pi}{6}}w_\zeta & e^{-i\frac{2\pi}{6}}w_\zeta^* & \frac{s}{\sqrt{3}}-s\frac{q_x+\sqrt{3}q_y}{2b}\end{pmatrix},$$

$$w_\zeta\approx\frac{1}{2}\Big[\Big(u_0-2s\zeta u_1+\sqrt{3}\zeta u_3\Big)+i\zeta\Big(\tilde{u}_0+2s\zeta\tilde{u}_1-\sqrt{3}\zeta\tilde{u}_3\Big)\Big]. \quad (4)$$

For $w_\zeta\neq 0$, the inversion-symmetric terms in Eq. (4) partially lift the $\zeta\boldsymbol{\kappa}$-point degeneracy into a singlet with energy $E_{\boldsymbol{\kappa}}-2w_\zeta$ and a doublet with energies $E_{\boldsymbol{\kappa}}+w_\zeta$, so that a distinctive mDP [9, 22] characterised by Dirac

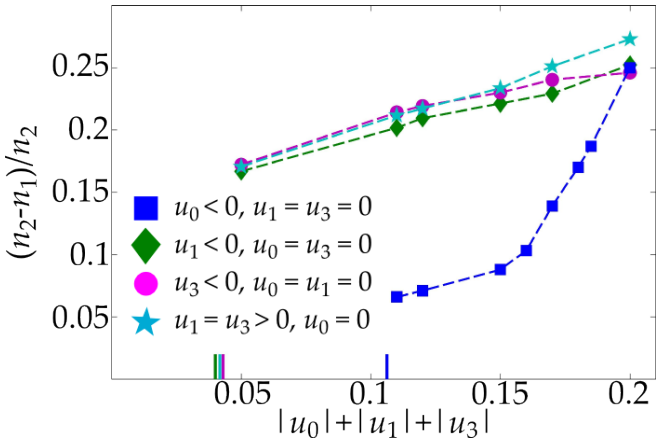

FIG. 3: The relation between the two densities at which the Hall coefficient in graphene reverses sign upon it's doping with holes. The results are shown for several realisations of moiré superlattice in the parameter range corresponding to either three isolated mDPs on the sBZ edge (squares) or one isolated mDP at the sBZ corner (other symbols). The thresholds for isolation are indicated on the x-axis.

velocity $v_{\boldsymbol{\kappa}}=[1+O(u)]\,\frac{v}{2}$ is always present at $\pm\boldsymbol{\kappa}$ somewhere in the spectrum [23]. Note that each isolated mDP is surrounded by Van Hove singularities in the density of states corresponding to saddle points in the lowest energy minibands, and, that the presence of the weaker inversion-asymmetric perturbation is able to open a minigap in the mDPs.

Also, the appearance of mDPs at the edge of the first miniband results in a peculiar spectrum of electronic Landau levels, as shown on the r.h.s of Fig. 2. Each data point in these spectra represents one of the Hofstadter minibands [24] (with an indistinguishably small width) calculated for rational values of magnetic flux, $\frac{p}{q}\Phi_0$ per moiré supercell following a method in Ref. [13]. Using these spectra one can trace a clearly separated "zero-energy" Landau level related to the isolated $\boldsymbol{\kappa}$-point mDP in the valence band in the bottom row of Fig. 2, in addition to the true zero-energy Landau level at the conduction-valence band edge. The three isolated mDPs on the sBZ edge in the valence band (top row of Fig. 2) also results in a "zero-energy" Landau level, though not as clearly separated and split by the magnetic breakdown occurring at $\Phi\approx 0.1\Phi_0$.

To summarise, the inversion symmetric moiré perturbation will result in either the first sBZ separated from the rest of the spectrum by one or three mDPs, or, for weak perturbations, will result in overlapping first and higher minibands. The experimental consequences of this can be expected in the optical spectroscopy of graphene on a hexagonal substrate: the presence of mDPs and Van Hove singularities in the density of states should lead to a modulation of the FIR and IR absorption spectra of monolayer graphene, which otherwise, has the flat absorption coefficient of 2.3%. Another experimental consequence of the moiré minibands would consist in a non-monotonic variation of the Hall coefficient upon doping the graphene flake with electrons or holes. For example, for those miniband spectra in Fig. 2, where there are isolated mDPs in the valence band, the Hall coefficient would pass through a zero value and change sign at two characteristic Hall densities, n_1 and n_2. At the density n_1 which corresponds to the valence band filled with holes up to the Van Hove singularity the Hall coefficient will change sign from positive to negative. At the higher Hall density, n_2, which corresponds to a completely filled first miniband, it would repeat the behaviour at the neutrality point changing sign from negative to positive. Such behaviour is expected to take place for the entire regions of the parametric space painted red, blue or green in Fig. 1. The relation between these two carrier densities for various types and strengths of moiré perturbations is shown in Fig. 3. For the clear part of the parametric space for which we find substantial overlap between many moiré minibands such alternations in the sign of the Hall coefficient would be obscured by the competing contributions from the "electron-like" and "hole-like" branches in the spectrum.

The authors thank F. Guinea, A. MacDonald and P.

San-Jose for useful discussions during the 2012 KITP programme *The Physics of Graphene*, when this study was started. We acknowledge financial support from DTC NOWNANO, ERC Advanced Grant *Graphene and Beyond*, EU STREP *ConceptGraphene*, Royal Society Wolfson Research Merit Award and EPSRC Science and Innovation Award.

[1] C. R. Dean, A. F. Young, I. Meric, C. Lee, L. Wang, S. Sorgenfrei, K. Watanabe, T. Taniguchi, P. Kim, K. L. Shepard, and J. Hone, Nature Nanotech. **5**, 722 (2010).

[2] J. Xue, J. Sanchez-Yamagishi, D. Bulmash, P. Jacquod, A. Deshpande, K. Watanabe, T. Taniguchi, P. Jarillo-Herrero, and B. J. LeRoy, Nature Mater. **10**, 282 (2011).

[3] R. Decker, Y. Wang, V. W. Brar, W. Regan, H.-Z. Tsai, Q. Wu, W. Gannett, A. Zettl, and M. F. Crommie, Nano Lett. **11**, 2291 (2011).

[4] A. S. Mayorov, R. V. Gorbachev, S. V. Morozov, L. Britnell, R. Jalil, L. A. Ponomarenko, P. Blake, K. S. Novoselov, K. Watanabe, T. Taniguchi, and A. K. Geim, Nano Lett. **11**, 2396 (2011).

[5] E. Kim, T. Yu, E. S. Song, B. Yu, Appl. Phys. Lett. **98**, 262103 (2011).

[6] H. Wang, T. Taychatanapat, A. Hsu, K. Watanabe, T. Taniguchi, P. Jarillo-Herrero, and T. Palacios, IEEE Electron Device Lett. **32**, 1209 (2011).

[7] M. S. Bresnehan, M. J. Hollander, M. Wetherington, M. LaBella, K. A. Thurnbull, R. Cavalero, D. W. Snyder, and J. A. Robinson, ACS Nano **6**, 5234 (2012).

[8] M. Yankowitz, J. Xue, D. Cormode, J. D. Sanchez-Yamagishi, K. Watanabe, T. Taniguchi, P. Jarillo-Herrero, P. Jacquod, and B. J. LeRoy, Nature Phys. **8**, 382 (2012).

[9] C. Ortix, L. Yang, and J. van den Brink, Phys. Rev. B **86**, 081405 (2012).

[10] M. Kindermann, B. Uchoa, D. L. Miller, Phys. Rev. B **86**, 115415 (2012).

[11] J. M. B. Lopes dos Santos, N. M. R. Peres, and A. H. Castro Neto, Phys. Rev. Lett. **99**, 256802 (2007).

[12] R. Bistritzer and A. H. MacDonald, Phys. Rev. B **81** 245412 (2010).

[13] R. Bistritzer and A. H. MacDonald, Phys. Rev. B **84** 035440 (2011).

[14] J. M. B. Lopes dos Santos, N. M. R. Peres, and A. H. Castro Neto, Phys. Rev. B **86**, 155449 (2012).

[15] S. V. Iordanskii and A. Koshelev, JETP Lett. **41**, 574 (1985).

[16] M. S. Foster and A. W. W. Ludwig, Phys. Rev. B **73**, 155104 (2006).

[17] A. F. Morpurgo and F. Guinea, Phys. Rev. Lett. **97**, 196804 (2006).

[18] J. C. Slonczewski and P. R. Weiss, Phys. Rev. **109**, 272 (1958).

[19] I. L. Aleiner and K. B. Efetov, Phys. Rev. Lett. **97**, 236801 (2006).

[20] The Hamiltonian in the vicinity of other two inequivalent points on the sBZ edge, $\boldsymbol{\mu}' = \hat{R}_{2\pi/3}\boldsymbol{\mu}$, $\boldsymbol{\mu}'' = \hat{R}_{4\pi/3}\boldsymbol{\mu}$, can be obtained using $H_{\boldsymbol{\mu}+\boldsymbol{q}} = H_{\boldsymbol{\mu}'+\hat{R}_{2\pi/3}\boldsymbol{q}} = H_{\boldsymbol{\mu}''+\hat{R}_{4\pi/3}\boldsymbol{q}}$.

[21] C.-H. Park, L. Yang, Y.-W. Son, M. L. Cohen, and S. G. Louie, Phys. Rev. Lett. **101**, 126804 (2008).

[22] F. Guinea and T. Low, Phil. Trans. R. Soc. A **368**, 5391 (2010).

[23] Note that the spectra derived from Eq. (4) obey the three-fold rotational symmetry.

[24] D. R. Hofstadter, Phys. Rev B **14**, 2239 (1976).